

Magnetic interactions in intercalated transition metal dichalcogenides: A study based on *ab initio* model construction

Tatsuto Hatanaka ^{1,*}, Takuya Nomoto ^{2,†} and Ryotaro Arita ^{2,3,‡}

¹*Department of Applied Physics, The University of Tokyo, Hongo, Bunkyo-ku, Tokyo 113-8656, Japan*

²*Research Center for Advanced Science and Technology, University of Tokyo, Komaba Meguro-ku, Tokyo 153-8904, Japan*

³*RIKEN Center for Emergent Matter Science (CEMS), Wako 351-0198, Japan*



(Received 21 November 2022; revised 8 March 2023; accepted 24 April 2023; published 15 May 2023)

Transition metal dichalcogenides (TMDs) are known to have a wide variety of magnetic structures by hosting other transition metal atoms in the van der Waals gaps. To understand the chemical trend of the magnetic properties of the intercalated TMDs, we perform a systematic first-principles study for 48 compounds with different hosts, guests, and composition ratios. Starting with calculations based on spin density functional theory, we derive classical spin models by applying the local force method to the *ab initio* Wannier-based tight-binding model. We show that the calculated exchange couplings are overall consistent with the experiments, and the chemical trend can be understood in terms of the occupation of the $3d$ orbital in the intercalated transition metal. The present results give us a useful guiding principle to predict the magnetic structure of compounds that are yet to be synthesized.

DOI: [10.1103/PhysRevB.107.184429](https://doi.org/10.1103/PhysRevB.107.184429)

I. INTRODUCTION

Transition metal dichalcogenides (TMDs) are two-dimensional layered materials of the type TX_2 , where T is a transition metal atom, and X is a chalcogen atom. They offer a fascinating playground to study various physical phenomena such as unconventional superconductivity, exotic charge density waves, emerging spin, valley, and exciton physics [1–4]. One of their characteristic features in bulk and thin films with atomic-scale thickness is that they can serve as an intercalation host. Namely, various guest elements can be accommodated in the van der Waals (vdW) gaps between each layer of TX_2 , changing the physical properties of the system dramatically. In particular, when $3d$ transition metal atoms (M) are intercalated a variety of magnetic states, such as helical spin states [5–10], half-metallic states [11], noncollinear antiferromagnetic states [12,13], and anisotropic in-plane ferromagnetic states [14,15], emerges for which intriguing transport phenomena like the anomalous Hall effect [16–18] and crystalline Hall effect [19] have been investigated intensively.

It is an interesting question whether such various magnetic states and properties realized in the intercalated TMDs can be reproduced from first principles and described/understood in terms of a simple model. It is also a nontrivial challenge to predict unknown magnetic properties for compounds that are yet to be synthesized. For these problems, recently, several *ab initio* studies have been performed. For example, a calculation based on density functional theory (DFT) has

successfully shown that the most stable state in $M_{1/3}NbS_2$ where $M=(Fe, Co)$ has a noncoplanar magnetic structure for which the topological Hall effect is expected to be observed [20]. For $M=(Cr, Mn, Fe)$, effective spin models were derived from first principles, and the origin of the characteristic helical magnetic structure has been discussed [21]. However, the general chemical trend of the host and guest dependence of the magnetic property of the intercalated TMDs is yet to be fully understood, and a systematic study for various host TX_2 and guest M with different composition ratios is highly desired.

To determine the most stable magnetic structure for a given material, there are several established approaches. One is of course a calculation based on spin DFT (SDFT), which usually works successfully for transition metal compounds [22]. However, this approach is numerically expensive and not so efficient when the magnetic unit cell is large. Another promising approach is deriving a classical spin model from SDFT calculation for a magnetic state (typically the ferromagnetic state) for which the numerical cost is not so expensive. Once a classical spin model is derived, we can determine the stable magnetic structures even when the magnetic unit cell is large.

The local force method, equivalently called the Liechtenstein formula [23], is often used to construct such effective spin models. With this method, we can evaluate the exchange interactions in the spin model by estimating the energy change against spin rotations. This formula has been successfully applied to the calculations for the magnetic transition temperatures of transition metals [24], noncollinear magnets, and magnetic alloys [25]. While it was originally formulated for the multiple scattering theory with the Green's functions and implemented in SDFT calculations with the Korringa-Kohn-Rostoker (KKR) theory, it is applicable to the tight-binding model based on *ab initio* Wannier functions [26–28].

*hatanaka-tatsuto346@g.ecc.u-tokyo.ac.jp

†nomoto@ap.t.u-tokyo.ac.jp

‡arita@riken.jp

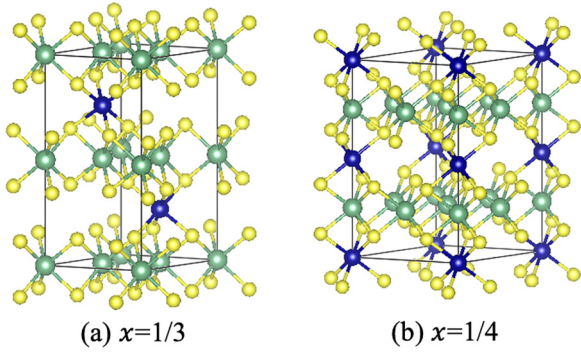


FIG. 1. Crystal structures of intercalated TMDs M_xTX_2 (a) for $x = 1/3$ and (b) for $x = 1/4$. Green, yellow, and blue spheres represent T , X , and M elements, respectively.

In this study, we first performed a systematic SDFT calculation for M_xTX_2 where $M = (\text{V}, \text{Cr}, \text{Mn}, \text{Fe}, \text{Co}, \text{Ni})$, $T = (\text{Nb}, \text{Ta})$, and $X = (\text{S}, \text{Se})$ with $x = 1/3$ and $1/4$ (48 compounds in total). Starting with the calculations for the representative ferromagnetic state of Cr_xTX_2 , we construct classical spin models by applying the local force method to the Wannier-based tight-binding model. We then determine the most stable magnetic structure for each material by examining the sign of the exchange interactions. In this approach, we discuss the possibility of the intralayer AF states, which are numerically expensive to investigate by SDFT calculation. We show that the theoretical results agree well with the magnetic orders experimentally reported. Moreover, we find that a simple model can give a unified explanation for the material dependence of the stable spin configuration in terms of the filling of the $3d$ orbitals of the intercalated transition metals. This observation gives us a useful guiding principle to predict magnetic properties of intercalated TMDs which are yet to be synthesized.

II. METHOD

A. Spin density functional theory

In our calculation scheme, the SDFT calculation is performed first. Then, based on the results, we construct a tight-binding Hamiltonian using the Wannier function. After that, we apply the local force method to the tight-binding Hamiltonian and derive the effective spin model. Finally, the stable magnetic order was determined. The results of magnetic order based on the effective spin model were compared with the experimental results and SDFT calculations for each compound.

We show the crystal structures of intercalated TMDs in Fig. 1. There are two intercalated transition metals per unit cell, which are located in different vdW gaps. The intercalated transition metals are surrounded by a distorted octahedron formed by chalcogen atoms. We can also see that intercalated transition metals form a hexagonal close-packed lattice when $x = 1/3$ and a triangular lattice stacked along the c axis when $x = 1/4$. In the SDFT calculation, we performed structural optimization for all target compounds. In this optimization, we assumed that the spin configuration is ferromagnetic (FM), and the lattice parameters and internal coordinates were

optimized, keeping the original space group symmetries $P6_322$ for $x = 1/3$ and $P6_3/mmc$ for $x = 1/4$.

The results of the stable magnetic order of the SDFT calculation were obtained by comparing the energies of the FM and AFM states for optimized structures of each compound. As mentioned before, there are two intercalated transition metals per unit cell (see Fig. 1). In the SDFT calculations, we focus on the magnetic structures that do not expand the unit cell. Thus, we consider only the antiferromagnetic (AFM) state having the interlayer antiferromagnetic and intralayer ferromagnetic structure.

B. Local force method

In the local force method, each of the exchange interactions (J_{ij}) are perturbatively evaluated by rotating a spin from the ferromagnetic state and examining the changes of the total energy. Here, we summarize a formulation based on the Wannier tight-binding models following Ref. [26]. Let us first consider the classical Heisenberg Hamiltonian:

$$H_s = -2 \sum_{\langle i,j \rangle} J_{ij} \mathbf{s}_i \cdot \mathbf{s}_j, \quad (1)$$

where $\langle i, j \rangle$ means all combinations of $i, j (i \neq j)$. We then introduce δE_{ij} as the energy change when we rotate the spin at site i by θ_i and site j by θ_j on the same rotation axis from the ferromagnetic state. It should be noted that δE_{ij} is directly related with the exchange interaction:

$$\frac{\partial^2 \delta E_{ij}}{\partial \theta_i \partial \theta_j} = -2J_{ij}. \quad (2)$$

Next, we consider the tight-binding Hamiltonian defined as follows,

$$H_{\text{TB}} = \sum_{1,2} A_{12} c_1^\dagger c_2, \quad (3)$$

where the indices 1,2 run over all degrees of freedom that specify the Wannier functions, namely, site i , atomic or molecular orbital ℓ , and spin σ indices. Using the Green's function for the tight-binding Hamiltonian, we can calculate the energy change due to the spin rotation. In the Green's functions formalism, the free energy F of the system (4) is expressed as

$$F = -T \sum_{\omega_n} e^{i\omega_n 0^+} \text{Tr} \ln[G^{-1}(i\omega_n)], \quad (4)$$

where $\omega_n = (2n + 1)\pi/\beta$ denotes the electronic Matsubara frequency, and the Green's function G is given by $G_{12}^{-1}(i\omega_n) = (i\omega_n \delta_{12} - A_{12})$. Generally, A_{12} can be divided into a time-reversal symmetric term t_{12} and antisymmetric term v_{12} . Here, following Ref. [26], we assume that v_{12} is local and can be expressed as $v_{i_1 \ell_1 \sigma_1, i_2 \ell_2 \sigma_2} = \delta_{i_1 i_2} B_{\ell_1 \ell_2}^i \sigma_{\sigma_1 \sigma_2}^z$ in a collinear magnetic phase, where B_i stands for the effective magnetic field, namely, the spin splitting in the tight-binding model. Here we use the atomic unit, i.e., the Bohr magneton $\mu_B = 1/2$.

If we rotate the spins as in the case of the Heisenberg model, the changes in the free energy, i.e., δF_{ij} , is given by

the following equation:

$$\frac{\partial^2 \delta F_{ij}}{\partial \theta_i \partial \theta_j} = T \sum_{\omega_n} \text{Tr}_\ell [B_i G_{ij}^{\uparrow\uparrow}(i\omega_n) B_j G_{ji}^{\downarrow\downarrow}(i\omega_n)]. \quad (5)$$

Here, $G_{ij}^{\sigma\sigma}(i\omega_n)$ is defined as a submatrix of $G_{12}(i\omega_n)$ with (i, j) site and (σ, σ) spin components. Tr_ℓ is a restricted trace for the ℓ index. By comparing these expressions with Eq. (2), we can evaluate J_{ij} for the itinerant Hamiltonian [Eq. (4)]:

$$J_{ij} = -\frac{T}{2} \sum_{\omega_n} \text{Tr}_\ell [B_i G_{ij}^{\uparrow\uparrow} B_j G_{ji}^{\downarrow\downarrow}]. \quad (6)$$

III. COMPUTATIONAL DETAILS

A. DFT calculation

We used the Vienna *Ab initio* Simulation Package (VASP) code [29] for SDFT calculations of intercalated TMDs. The Perdew-Burke-Ernzerhof exchange-correlation functional [30] and the projector augmented wave method [31,32] were used.

For materials having no magnetization in the SDFT calculations, we performed SDFT+ U calculations. The value of U was set as $U = 3$ eV for $\text{Fe}_{1/4}\text{XSe}_2$ ($X = \text{Nb}$ and Ta), the Co-, and Ni-intercalated compounds. The effects of the value of U are discussed in Appendix A. The energy cutoff for the plane-wave basis set was set to 500 eV, and a $12 \times 12 \times 8$ k -point grid for the primitive cell of the intercalated TMDs was used in the structural optimization and the calculations of the ground-state energies.

B. Construction of Wannier-based tight-binding model

Wannier functions were constructed by using the WANNIER90 code [33]. In Fig. 2, we show the band structures of $\text{Cr}_{1/3}\text{NbS}_2$ as a representative example. The inner window to fix the low-energy band dispersion was set from -8 to 2 eV. The energy cutoff for the plane-wave basis was set to 500 eV. A $12 \times 12 \times 8$ k -point grid was used in calculating FM reference states, and a $6 \times 6 \times 4$ sampling k -point grid was used for constructing Wannier functions.

C. Evaluation of exchange interactions

We applied the local force method to the Cr-intercalated compounds, and the exchange interactions for the other transition metal-intercalated compounds were evaluated by shifting the Fermi level, which corresponds to the rigid band approximation. In order to validate this approximation, we show the band structures of $M_x\text{NbS}_2$ in Appendix B. According to the results of the DFT calculation, only intercalated transition metals have a sizable magnetic moment, and those of the other atoms are negligibly small in the FM order. Thus we ignored interactions other than those between intercalated transition metals and extracted the spin model, whose interactions are finite only between intercalated transition metals. This approach works most successfully for the case in which Cr is intercalated. In other cases, spin polarization in the host TMD makes the applicability of the rigid-band approximation worse.

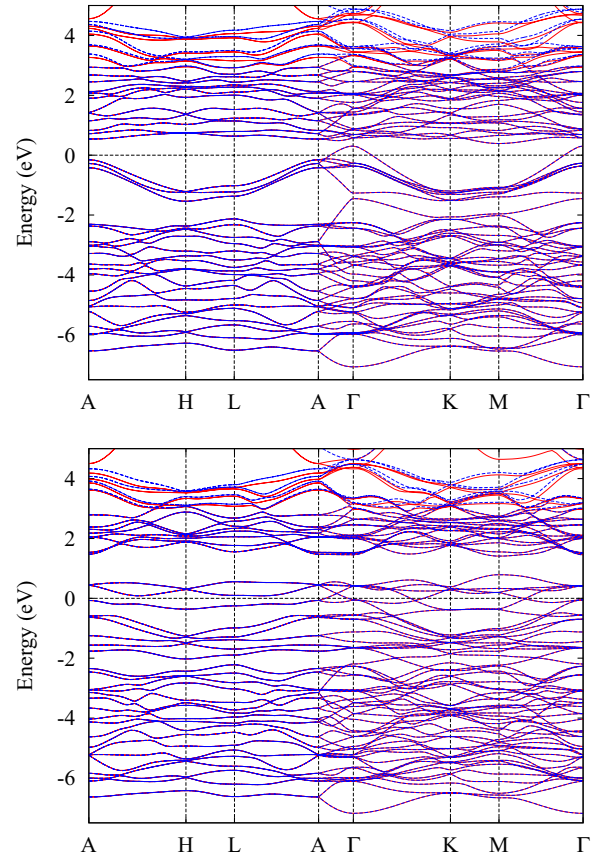


FIG. 2. Band structures of (upper) majority spin and (lower) minority spin of $\text{Cr}_{1/3}\text{NbS}_2$ in the ferromagnetic state. The energy is measured from the Fermi level. Blue lines are calculated from DFT calculations, and red lines are from the Wannier functions.

An $8 \times 8 \times 8$ k -point grid was used in the evaluation of Eqs. (5) and (6). Inverse temperature β was set to 500 eV^{-1} . In order to reduce the computational cost, we use the intermediate representation of the Green's function [34,35] in the local force method.

IV. RESULTS AND DISCUSSION

A. Stable magnetic order according to DFT calculation

We first summarize the experimentally observed magnetic structures in Table I. Table II shows the results of the DFT calculations, where we compare the energies of the FM and AFM states. We can see from Tables I and II that the experimental magnetic structures in 13 out of the 23 compounds are successfully reproduced in the DFT calculations. For three compounds that exhibit helimagnetic structures, namely $\text{Cr}_{1/3}\text{NbS}_2$, $\text{Mn}_{1/3}\text{NbS}_2$, $\text{Cr}_{1/3}\text{TaS}_2$, and $\text{Mn}_{1/4}\text{NbSe}_2$, the discrepancy is due to the nonrelativistic approximation where the spin-orbit coupling is absent. The remaining six compounds except for $\text{Fe}_{1/4}\text{TaS}_2$ (namely, $\text{Co}_{1/3}\text{NbS}_2$, $\text{Co}_{1/3}\text{TaS}_2$, $\text{Cr}_{1/4}\text{NbS}_2$, $\text{Cr}_{1/4}\text{NbSe}_2$, and $\text{Fe}_{1/4}\text{NbSe}_2$) are known to be AFM in the experiments but predicted to be FM in the DFT calculation. It should be noted that we did not consider intralayer AFM states in the DFT calculation because the magnetic unit cell becomes too large. Thus the intralayer

TABLE I. Stable magnetic structure in the experiments. F, HM, and AF stand for ferromagnetic, helimagnetic, and antiferromagnetic structures, respectively.

	$x = 1/3$						$x = 1/4$					
	V	Cr	Mn	Fe	Co	Ni	V	Cr	Mn	Fe	Co	Ni
NbS ₂	AF [36,37]	HM [5,8,9]	HM [9]	AF [38,39]	AF [12,40,41]	AF [42]	NbS ₂	– AF [46]	F [47,48]	AF [49,50]	–	–
NbSe ₂	–	F [6]	–	AF [43]	–	–	NbSe ₂	– AF [51]	HM [47]	AF [51,52]	–	–
TaS ₂	AF [37]	HM [10,14]	F [44]	F [17]	AF [12]	AF [45]	TaS ₂	–	– F [47,52]	F [18,53,54]	–	–
TaSe ₂	–	–	–	–	–	–	TaSe ₂	–	–	–	–	F [55]

magnetic structure is always FM, and only the interlayer magnetic structure can be AFM. We will see later in Table III that we obtain the correct AFM ground states in Cr_{1/4}NbS₂ and Cr_{1/4}NbSe₂ based on the spin model calculations derived by the local force method. On the other hand, in the case of Fe_{1/4}TaS₂, the AFM state is more stable than the FM state in the DFT calculation, while it is FM in the experiment. We will discuss this discrepancy in Sec. IV B.

B. Exchange constant

We show the filling (the number of electrons in the unit cell) dependence of the interlayer Figs. 3(a) and 3(b) and intralayer [Figs. 3(c) and 3(d)] exchange constants evaluated by the local force method. J_{intra} , J_{inter} are defined as the nearest-neighbor inter- and intralayer exchange interactions, respectively. It should be noted that we can calculate long-range interactions, including J_{intra} , even though we start with the calculation for a unit cell with one atom per plane because the spin rotation in evaluating J_{ij} is infinitesimally small. We here apply the nearest-neighbor approximation to the effective spin model and thereby only consider J_{intra} and J_{inter} . The effect of distant interactions is discussed in Appendix C. As we described in Sec. III C, we start with the most representative case, i.e., the ferromagnetic state for $M = \text{Cr}$. We shift the position of the Fermi level and look at the energy change due to a spin rotation. While we neglect the detail of the guest (M) dependence on the electronic structure, as we see below, the rigid-band approximation successfully reproduces the overall chemical trend of the experimental results.

Figures 3(a) and 3(c) are the results for $x = 1/3$, and Figs. 3(b) and 3(d) are those for $x = 1/4$. Let us first look at the former. We see that both the intralayer and interlayer interactions have a similar filling dependence. When the number of electrons is small or large, the exchange constants tend to take a positive small value (FM). On the other

hand, when the filling is close to half-filling (as in the cases of Mn, Fe, and Co), the interactions tend to be negative (AFM). This result is consistent with the previous study for the Fe- and Co-intercalated $x = 1/3$ system in which non-coplanar AFM structures were shown to be favored [20] since the hexagonal close-packed lattice is magnetically frustrated when all the nearest-neighbor interactions are negative. Note that higher-order exchange interactions could be important for this compound and discussed in Appendix D. Our result is also consistent with Ref. [21] where the fully relativistic Korringa-Kohn-Rostoker (KKR) Green's function method was employed, indicating that the present computational method works successfully and the effect of spin-orbit coupling is irrelevant.

Next, let us move on to the case of $x = 1/4$. We see that the interlayer exchange constant shown in Fig. 3(b) does not show a significant host (TX_2) dependence for $M = (\text{V}, \text{Cr}, \text{Mn}, \text{Fe})$. We see a similar behavior for the intralayer exchange constant [Fig. 3(d)]. Another distinct feature is that the energy scale of the intralayer exchange constant is much smaller than that of the interlayer exchange constant. Namely, the system has a strong coupling along the c axis rather than in the ab plane.

In Table III, we summarize the stable magnetic structures determined by the sign of the nearest-neighbor exchange constants. In both $x = 1/3$ and $1/4$ cases, the ferromagnetic order is stable only if both J_{inter} , J_{intra} are positive, and otherwise, antiferromagnetic order becomes stable. Among 23 compounds for which the magnetic structure is determined experimentally, we can say that the theoretical magnetic structures of 14 compounds are consistent with the experiment. Unlike SDFT calculations, we reproduce the stable magnetic order consistent with the experiment for Cr_{1/4}NbS₂ and Cr_{1/4}NbSe₂. As mentioned in Sec. IV A, when we do not expand the unit cell, we can only consider the simplest interlayer antiferromagnetic structure so that SDFT calculations

TABLE II. Stable magnetic structure in the DFT calculations. Letters with an asterisk (*) denote that the theoretical results are inconsistent with the experimental results in Table I. F and AF stand for ferromagnetic and antiferromagnetic structures, respectively. It should be noted that AF denotes the interlayer antiferromagnetic configuration.

	$x = 1/3$						$x = 1/4$						
	V	Cr	Mn	Fe	Co	Ni	V	Cr	Mn	Fe	Co	Ni	
NbS ₂	AF	F *	F *	AF	F *	AF	NbS ₂	F	F *	F	AF	AF	F
NbSe ₂	AF	F	F	AF	AF	AF	NbSe ₂	F	F *	F *	F *	AF	F
TaS ₂	AF	F *	F	F	F *	AF	TaS ₂	F	F	F	AF *	AF	F
TaSe ₂	F	F	F	AF	AF	AF	TaSe ₂	F	F	F	F	AF	F

TABLE III. Stable magnetic structure in the classical spin model derived by the local force method. Letters with an asterisk (*) denote that the theoretical results are inconsistent with the experimental results in Table I. F and AF stand for ferromagnetic and antiferromagnetic structures, respectively. F/AF means we do not specify stable magnetic order because at least $|J_{\text{inter}}|$ or $|J_{\text{intra}}|$ is smaller than 0.2 meV, and the Fermi level is located near the sign change of J_{ij} .

	$x = 1/3$						$x = 1/4$						
	V	Cr	Mn	Fe	Co	Ni	V	Cr	Mn	Fe	Co	Ni	
NbS ₂	AF	F *	F/AF *	AF	AF	F *	NbS ₂	AF	AF	F	AF	AF	AF
NbSe ₂	AF	F	F	AF	AF	F	NbSe ₂	AF	AF	F *	AF	AF	AF
TaS ₂	AF	F *	F/AF	AF *	AF	F *	TaS ₂	AF	AF	F	AF *	AF	AF
TaSe ₂	F/AF	F	AF	AF	AF	F	TaSe ₂	AF	AF	F/AF	AF	AF	AF *

take into account only the interlayer magnetic interactions. In the case of these three compounds, by including antiferromagnetic interactions in the intralayer direction, the accurate order was obtained. Here, let us note that both the interlayer and intralayer exchange constants change their sign around $M = \text{Mn}$. Thus we do not determine which magnetic order is stable for six compounds with $M = \text{Mn}$. Similarly, in the case of $\text{Ni}_{1/3}\text{NbS}_2$ and $\text{Ni}_{1/3}\text{TaS}_2$, at least one of the intralayer or interlayer interactions is close to zero, indicating that these materials are located near the boundary between the FM and AFM states.

On the other hand, for the case of Fe_xTaS_2 , our approach does not reproduce the experimental results. For $x = 1/3$, we should note that while SDFT apparently reproduces the ferromagnetic ground state in the experiment [17], the intralayer AFM state is not considered in the calculation. For $x = 1/4$,

neither the SDFT calculation nor the local force approach reproduces the experimental ferromagnetic ground states. One possible reason is the contribution of the orbital magnetization of the intercalated Fe atoms. While it is shown that intercalated Fe atoms have a finite orbital moment of about 33% of the spin moment [54], the orbital moment is not taken into account in the present calculation. Regarding the reason for the disagreement between theory and experiment, we leave it for future study.

C. Interpretation of the material dependence of the exchange constant

As we have seen in Fig. 3, the energy scale of the interlayer and intralayer exchange constants are similar to each other for $x = 1/3$ but very different for $x = 1/4$. This result

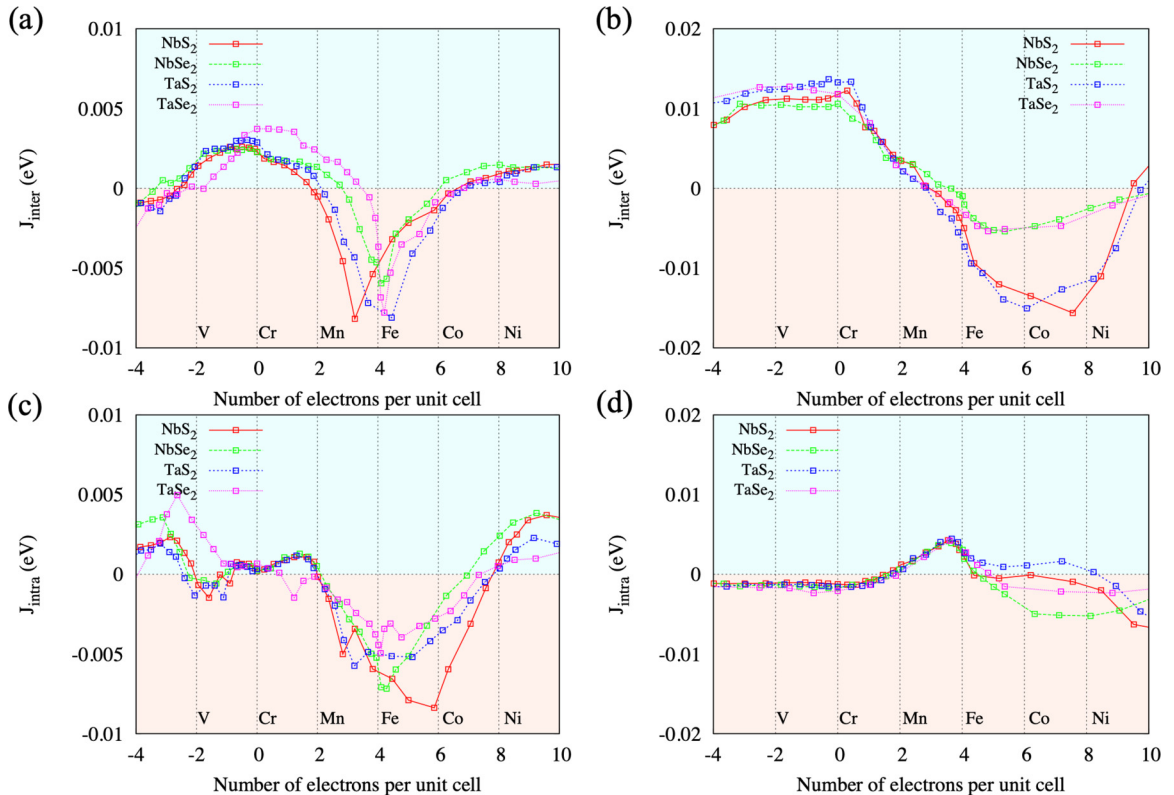


FIG. 3. Exchange constants evaluated by the local force method. Panels (a) and (c) are results for $x = 1/3$, and (b) and (d) are for $x = 1/4$. Six vertical black dotted lines correspond to the Fermi level of V-, Cr-, Mn-, Fe-, Co-, and Ni-intercalated compounds, respectively.

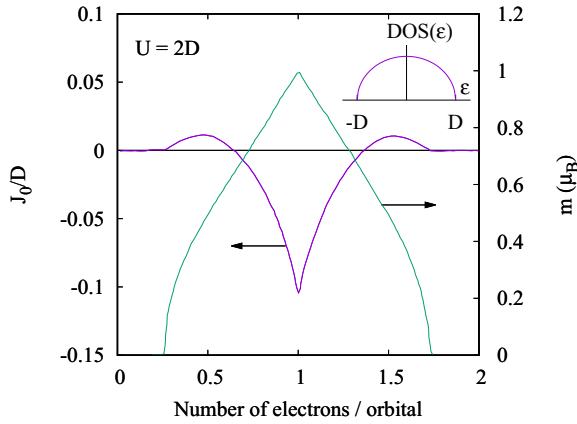


FIG. 4. Filling dependence of J_0 for the single-orbital Hubbard model on the Bethe lattice.

indicates that while the intercalated TMDs are crystallographically two-dimensional, they are magnetically isotropic (three-dimensional) for $x = 1/3$ but anisotropic (quasi-one-dimensional) for $x = 1/4$. In this subsection, let us discuss whether the material dependence of the exchange constant for intercalated TMDs can be understood in terms of a simple single-orbital Hubbard model on the Bethe lattice. When the Coulomb repulsion (the Hubbard U) is absent, the system has a semicircular DOS (see the inset of Fig. 4). We set the

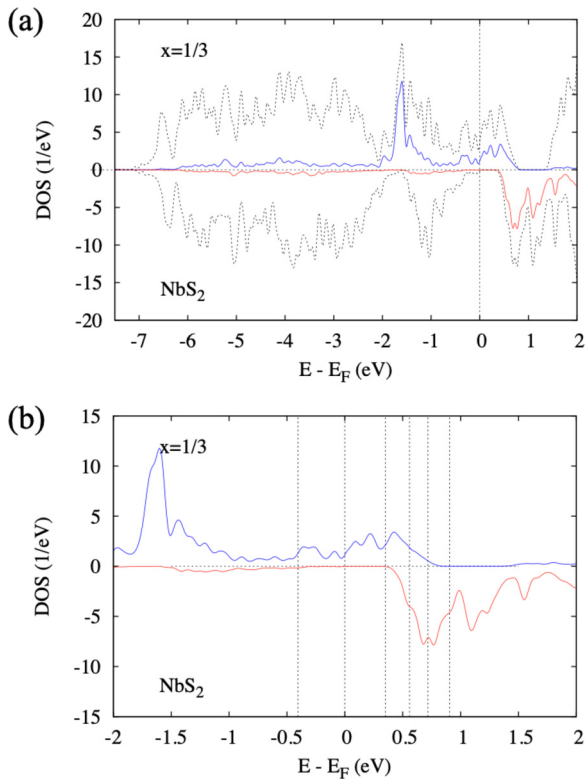


FIG. 5. (a) DOS and PDOS of the $3d$ orbitals for $\text{Cr}_{1/3}\text{NbS}_2$. Black dotted line is DOS and blue (red) line is the PDOS of the $3d$ orbitals with the majority (minority) spin. (b) Enlarged plot for the PDOS of the $3d$ orbitals. Six vertical black dotted lines denote the Fermi level of V-, Cr-, Mn-, Fe-, Co- and Ni-intercalated TMDs determined by the rigid band approximation.

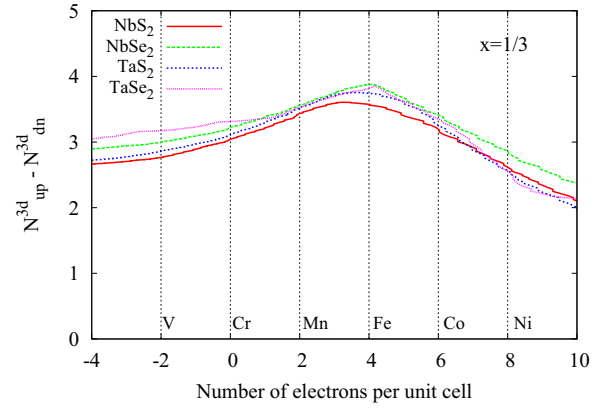


FIG. 6. Spin polarization (difference between the filling of the majority and minority spins) of the $3d$ orbitals in $M_{1/3}TX_2$.

bandwidth $W = 2D$ and $U = W$. In Fig. 4, we show the filling dependence of $J_0 (= \sum_{i \neq 0} J_{0i})$ [56]. When the filling is closed to 1 (half-filling), the super-exchange mechanism is dominant, and thus J_0 takes a negative value. On the other hand, when the filling is very low or high, the double exchange mechanism makes J_0 positive. Namely, the system is FM for low and high filling but AFM for half-filling. Interestingly, this behavior can be seen for both the interlayer and intralayer exchange constant for $x = 1/3$ [see Figs. 3(a) and 3(c)].

In Fig. 4, we also plot the spin polarization (i.e., the difference between the filling of the majority and minority spins) as a function of the filling. We see that AFM interaction is strongest when the spin polarization is the largest. It is interesting to see whether this behavior can also be seen for the exchange constants of $M_{1/3}TX_2$. As a typical case, let us look into the case of $\text{Cr}_{1/3}\text{NbS}_2$. In Fig. 5, we show the total DOS and partial DOS (PDOS) of the $3d$ orbitals. The vertical black dotted lines in Fig. 5(b) denote the Fermi level (E_F) for $M = \text{V}, \text{Cr}, \text{Mn}, \text{Fe}, \text{Co}$, and Ni from the left, respectively. We see that when $E_F = 0$ (i.e., the case of $M = \text{Cr}$), the minority spin is almost empty. When E_F is higher than that of Mn ($\sim 0.4\text{eV}$), the majority spin starts to be occupied. Thus the spin polarization takes its maximum between $M = \text{Mn}$ and Fe . To clarify this situation, in Fig. 6, we plot the spin polarization for $M_{1/3}\text{NbS}_2$ together with the results for other $M_{1/3}TX_2$. From these plots, we expect that the AFM interaction becomes strongest for $M = \text{Mn}$ or Fe , and indeed, it is the case seen in Figs. 3(a) and 3(c).

On the other hand, the filling dependence of the exchange interaction for $x = 1/4$ is apparently different from that for $x = 1/3$. This behavior can be explained in terms of the crystalline electric field (CEF) splitting. Here, it should be noted that the electronic structure of the $x = 1/4$ systems is quite anisotropic, and the amplitudes of the interlayer and intralayer interactions are very different.

Suppose there are five orbitals in an isotropic system. The five orbitals have the same energy level, and the system is considered to be half-filled when there are five electrons occupying each site. However, if the electronic structure is anisotropic, where the five energy levels are split into two high-energy states and three low-energy states, the system is (effectively) half-filled when eight electrons occupy each site,

TABLE IV. On-site energies (eV) of the Wannier functions for d orbitals of Cr_xNbS_2 measured from the Fermi energy.

x	$d_{3z^2-x^2}$	d_{zx}	d_{yz}	d_{xy}	$d_{x^2-y^2}$
1/3	0.052	0.092	0.099	0.175	0.129
1/4	-0.138	0.003	0.013	0.129	0.125

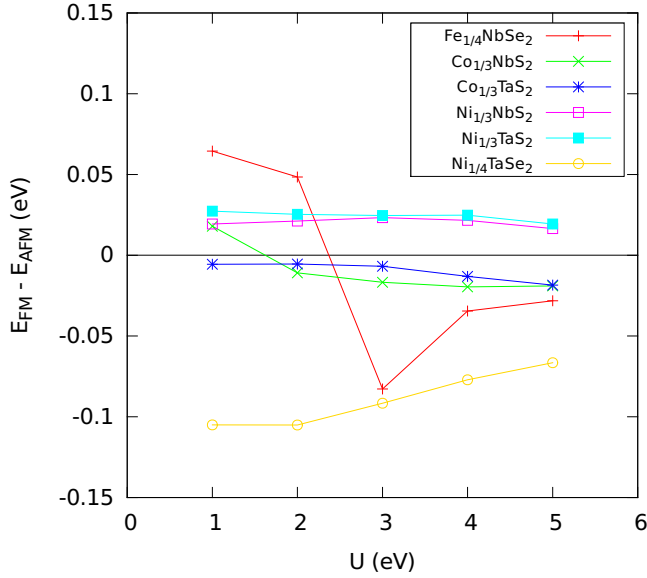


FIG. 7. U dependence of the energy differences between the ferromagnetic (E_{FM}) and antiferromagnetic (E_{AFM}) states.

with the two high-energy states being half-filled. Thus, in general, the antiferromagnetic interaction is not necessarily strong for Mn or Fe in anisotropic systems. Although this argument is for the limit of large CEF, it is helpful to understand the filling dependence of J_{inter} for $x = 1/4$. In fact, CEF plays a crucial role in determining the spin configuration when it is comparable to Hund's coupling [57]. In Table IV, we list the on-site energies of the $3d$ orbitals in Cr_xNbS_2 measured from the Fermi energy for $x = 1/3$ and $1/4$. We can see that the energy splitting in the $x = 1/4$ systems is larger than that in the $x = 1/3$ systems, which is a possible reason why J_{inter} does not take its minimum at $M = \text{Mn}$ or Fe . It should be noted that the ferromagnetic interaction is strong in the limit of low and high filling, which is a feature common to Fig. 3(a). On the other hand, the filling dependence of J_{intra} [Fig. 3(b)] is difficult to understand due to its small energy scale.

V. CONCLUSION

By means of first-principles calculations based on SDFT and *ab initio* derivation of the classical spin model based on the local force method, we systematically investigated the material dependence of the magnetic interactions in 48 intercalated TMDs $M_x\text{TX}_2$, in which a variety of magnetic structures is realized. For both $x = 1/3$ and $x = 1/4$, our calculations overall succeeded in reproducing the experimental results. We give a simple interpretation on the intercalated guest-atom dependence in terms of the filling of the $3d$ orbitals. The present result will provide a useful guideline to predict magnetic structures in compounds which have not been synthesized.

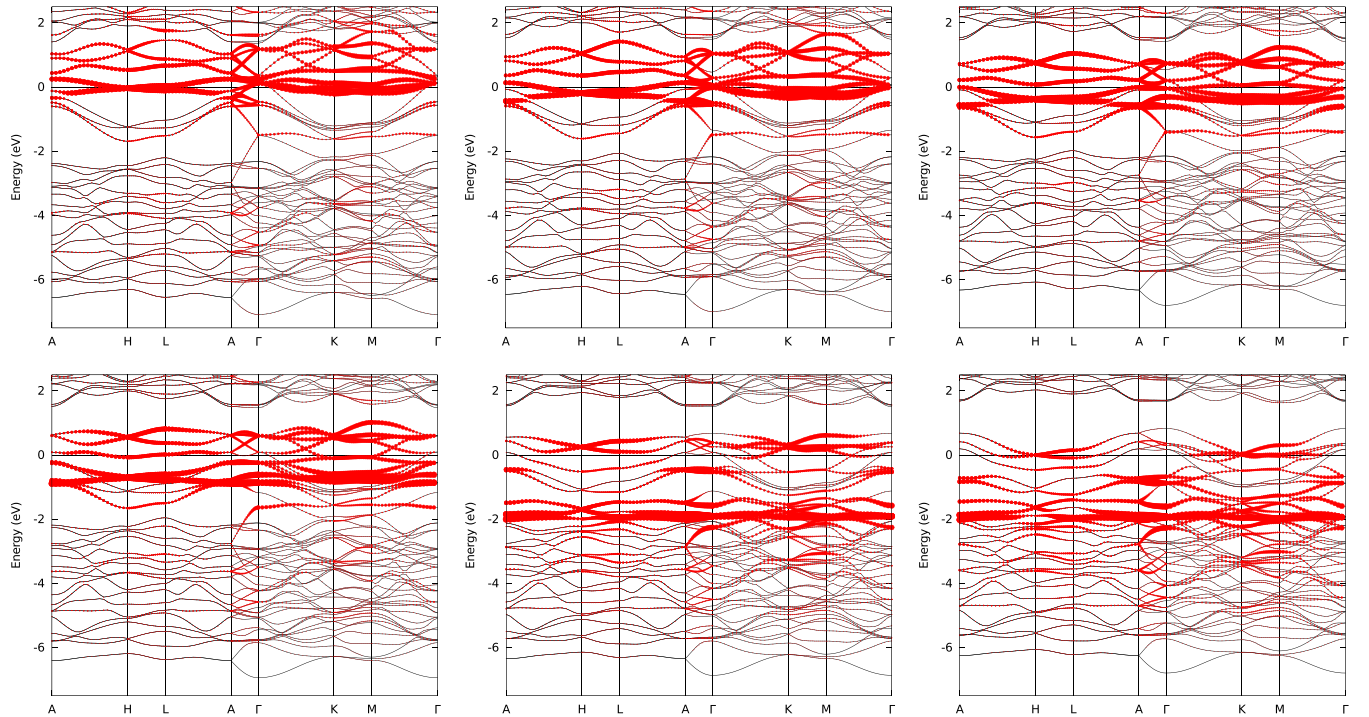


FIG. 8. Band structures of $M_{1/3}\text{NbS}_2$. Each figure corresponds to the band structure of $M = \text{V}, \text{Cr}, \text{Mn}, \text{Fe}, \text{Co},$ and Ni from the upper left to the lower right. SDFT+ U was applied for $M = \text{Co}$ and Ni cases. Black lines are the band structure of $M_{1/3}\text{NbS}_2$ and thickened red circles are the weight of $3d$ orbitals.

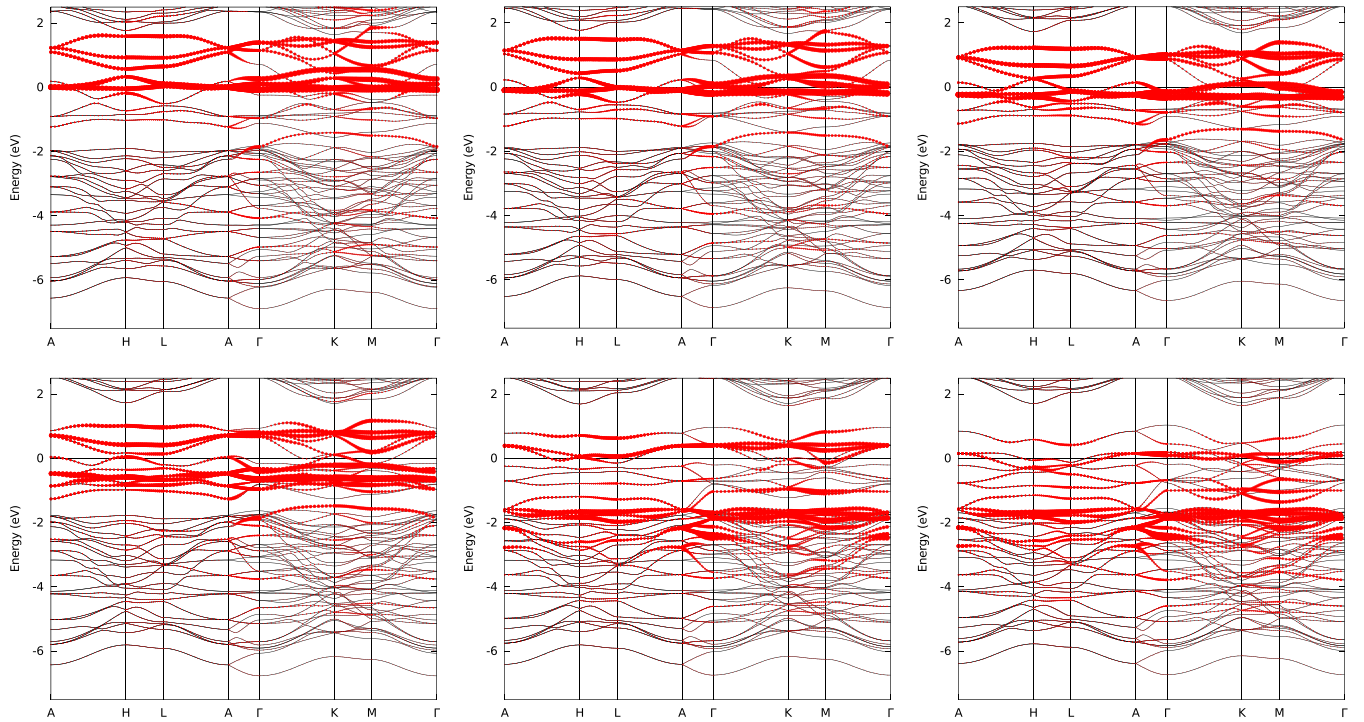


FIG. 9. Band structures of $M_{1/4}\text{NbS}_2$. Each figure corresponds to the band structure of $M = \text{V, Cr, Mn, Fe, Co, and Ni}$ from the upper left to the lower right. SDFT+ U was applied for $M = \text{Co and Ni}$ cases. Black lines are the band structure of $M_{1/4}\text{NbS}_2$ and thickened red circles are the weight of $3d$ orbitals.

ACKNOWLEDGMENTS

We would like to thank Masaki Nakano for illuminating discussions. We acknowledge financial support from Grants-in-Aid for Scientific Research (JSPS KAKENHI) Grants No. JP21H04437, No. JP21H04990, and No. JP19H05825. T.N. was supported by JST, PRESTO Grant No. JPMJPR20L7, Japan.

APPENDIX A: EFFECT OF THE VALUE OF U IN SDFT CALCULATION

In Sec. IV, we performed SDFT+ U calculation when SDFT did not find a ferromagnetic self-consistent solution. While the value of U was fixed to be 3 eV in Sec. IV, here we show the U dependence for the following compounds: $\text{Fe}_{1/4}\text{NbSe}_2$, $\text{Co}_{1/3}\text{NbS}_2$, $\text{Co}_{1/3}\text{TaS}_2$, $\text{Ni}_{1/3}\text{NbS}_2$, $\text{Ni}_{1/3}\text{TaS}_2$, and $\text{Ni}_{1/4}\text{TaSe}_2$, which we compared with the experimental results in Table I. As was done in Sec. IV, we optimized the atomic configuration and calculated the total energies of the FM and AFM states for $U=1,2,3,4$, and 5 eV (see Fig. 7). We can see that the energy relationship between the FM and AFM states does not sensitively depend on the U value except for $\text{Fe}_{1/4}\text{NbSe}_2$ and $\text{Co}_{1/3}\text{NbS}_2$. For $\text{Fe}_{1/4}\text{NbSe}_2$ and $\text{Co}_{1/3}\text{NbS}_2$, as was shown for $\text{Fe}_{1/3}\text{NbSe}_2$ (Ref. [58]), the AFM state observed in the experiment is stable for U smaller than ~ 3 eV.

APPENDIX B: BAND STRUCTURES OF INTERCALATED TMD AND THE VALIDITY OF THE RIGID BAND APPROXIMATION

We show the band structures of the paramagnetic state of $M_x\text{NbS}_2$ in Figs. 8 and 9, and the band structures for other

host TMDs hardly change. As we can see in Figs. 8 and 9, in the energy window of ± 2 eV, there are bands that originate from the intercalated transition metal atoms. The dispersion is very similar to each other, justifying the validity of the rigid band approximation.

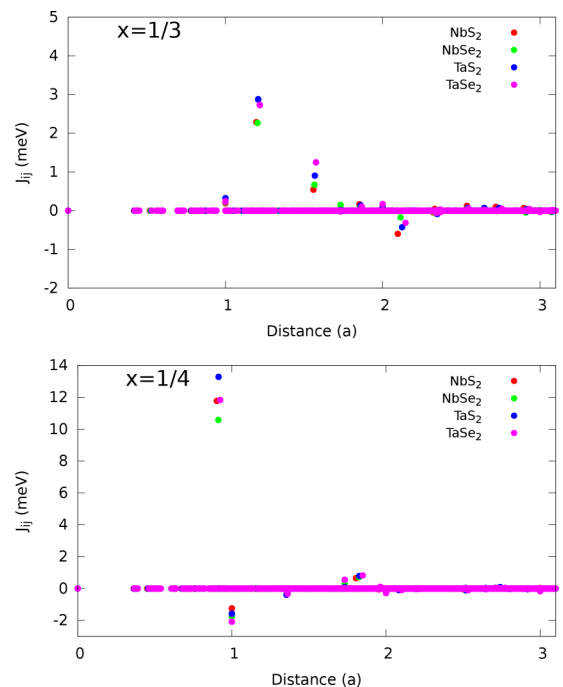
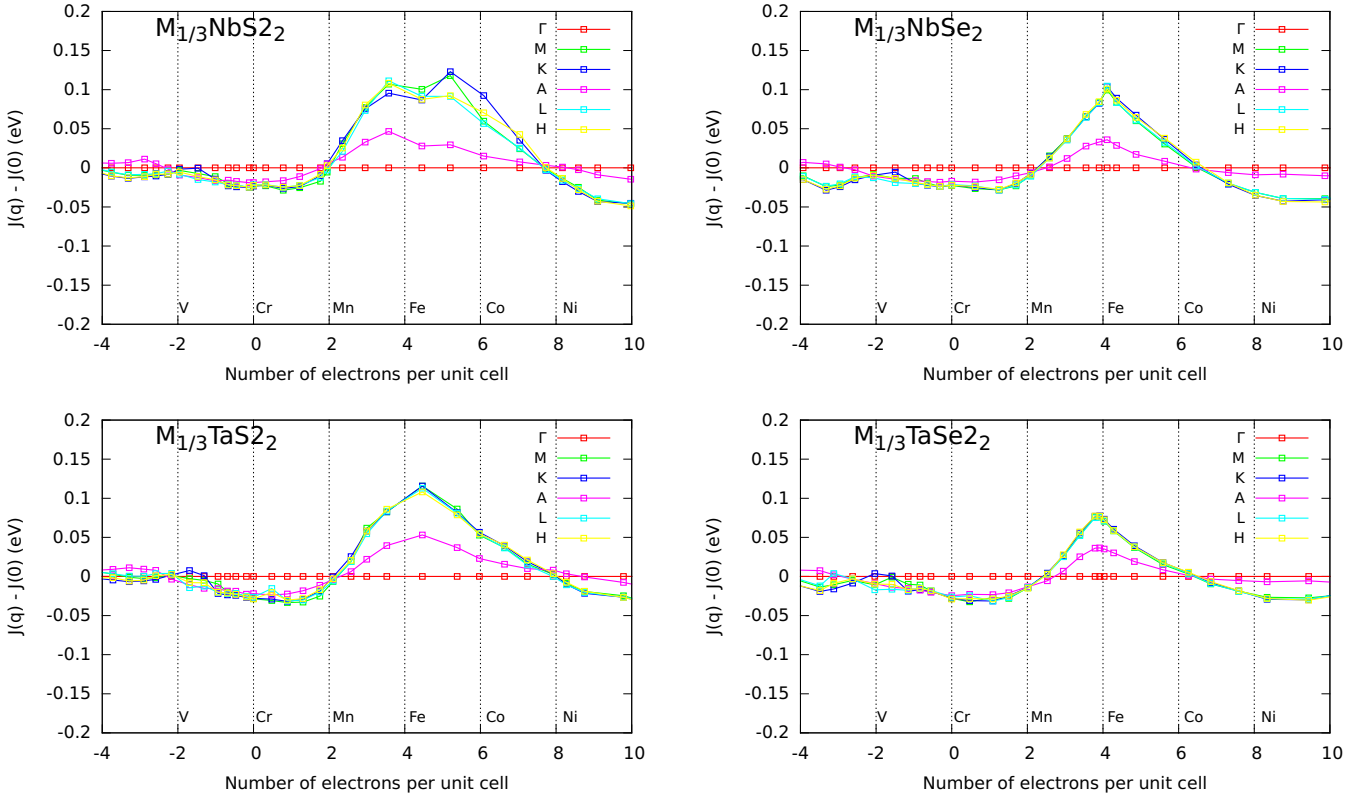


FIG. 10. Distance dependence of the exchange interactions in $\text{Cr}_{1/3}\text{TX}_2$ and $\text{Cr}_{1/4}\text{TX}_2$. The horizontal axis is normalized by the lattice constant along the a axis for each compound.


 FIG. 11. Exchange interactions in the reciprocal space $J(\mathbf{q})$ for $x = 1/3$ systems.

APPENDIX C: EFFECT OF DISTANT EXCHANGE INTERACTIONS

In Sec. IV, we employed the nearest-neighbor (NN) approximation to determine the stable magnetic structure. In this Appendix, we discuss the effect of the distant exchange interactions on the magnetic structure. In Fig. 10, we show the distance dependence of the exchange interactions $J(|\mathbf{R}|)$ for $\text{Cr}_{1/3}\text{TX}_2$ and $\text{Cr}_{1/4}\text{TX}_2$. The distance $|\mathbf{R}|$ between the site i and j is normalized by the lattice constant along the a axis for each compound. While only the NN exchange interaction is dominant and the others are tiny in the $x = 1/4$ systems, the second and third NN interactions have a comparable magnitude for the $x = 1/3$ systems. Let us now look into the effect of these distant interactions on the stable magnetic structure. Note that we used $8 \times 8 \times 8$ k -point grid in the local force method so that the exchange interactions in the real space $J(\mathbf{R})$ up to $|\mathbf{R}| = 4$ are considered. In Fig. 10, we can confirm that $|J(\mathbf{R})|$ is sufficiently small and can be neglected for $|\mathbf{R}| > 3$. The exchange interactions in the reciprocal space $J(\mathbf{q})$ are calculated as

$$J(\mathbf{q}) = \sum_{\mathbf{R}} J(\mathbf{R}) e^{-i\mathbf{q} \cdot \mathbf{R}}. \quad (\text{C1})$$

In Fig. 11, we plot the exchange interactions $J(\mathbf{q})$ of the $x = 1/3$ compounds at the high symmetry points in the first Brillouin zone measured from that at the Γ point $J(\mathbf{q} = \mathbf{0})$. When $J(\mathbf{q}) - J(\mathbf{0})$ takes a negative value for all \mathbf{q} , the system favors ferromagnetic states. We can see that while the ferromagnetic interaction at $\mathbf{q} = \mathbf{0}$ is dominant for the high- and

low-filling compounds, the antiferromagnetic interactions are stronger for the Fe- and Co-intercalated compounds. For $M = \text{Fe}$ and Co , it should be also noted that $J(\mathbf{q})$ takes similar values at different wave numbers, indicating that the spin configuration is severely frustrated. These results are consistent with the real-space analysis shown in Sec. IV B.

In Table V, we summarize the stable magnetic order determined from the magnitudes of the exchange interactions in the reciprocal space. By comparing the results with Table III, we can see that the long-range exchange interactions have no significant effects on the magnetic structure.

TABLE V. Stable magnetic structure in the classical spin model in the reciprocal space obtained from the real space spin model constructed by the local force method. Letters with an asterisk(*) denote that the theoretical results are not consistent with the experimental results in Table I. F, AF stand for ferromagnetic and antiferromagnetic structures, respectively, and F/AF means that the stable magnetic structure is not determined because the maximum exchange interaction of the wave vectors other than the Γ point is very close to that of the Γ point.

	V	Cr	Mn	Fe	Co	Ni
NbS ₂	F/AF	F *	F/AF *	AF	AF	F *
NbSe ₂	F/AF	F	F	AF	AF	F
TaS ₂	F/AF	F *	F/AF	AF *	AF	AF
TaSe ₂	F/AF	F	F	AF	AF	F

APPENDIX D: EFFECT OF HIGHER-ORDER EXCHANGE INTERACTION

We have performed spin model calculations by the Landau-Lifshitz-Gilbert (LLG) equation, including higher-order exchange interactions for some compounds. Primarily we give attention to the difference between $\text{Fe}_{1/3}\text{NbS}_2$ and $\text{Co}_{1/3}\text{NbS}_2$. Even though nearest-neighbor interactions are antiferromagnetic in both compounds, the former is reported to have the collinear AFM [38] in the ground state and the latter to have the noncoplanar AFM [20]. These two AFM structures degenerate as the ground state of the classical spin model with only quadratic interactions on the hexagonal-close-packed lattice. We considered the classical spin Hamiltonian with the quadratic interactions in the main text. As the most natural extension, we consider here the following Hamiltonian with biquadratic exchange interaction terms,

$$H_s = -2 \sum_{\langle i,j \rangle} J_{ij} \mathbf{s}_i \cdot \mathbf{s}_j - 2 \sum_{\langle i,j \rangle} B_{ij} (\mathbf{s}_i \cdot \mathbf{s}_j)^2, \quad (\text{D1})$$

where $\langle i, j \rangle$ means all combinations of i, j and we take into account only the nearest-neighbor interactions again. Then we simulated real-time and space dynamics of classical spins by the LLG equation given below,

$$\begin{aligned} \frac{\partial \mathbf{s}_i}{\partial t} &= -\mathbf{B}_i^{\text{eff}} \times \mathbf{s}_i - \frac{\alpha}{s} [\mathbf{s}_i \times (\mathbf{s}_i \times \mathbf{B}_i^{\text{eff}})], \\ \mathbf{B}_i^{\text{eff}} &= -\frac{\partial H_s}{\partial \mathbf{s}_i}, \end{aligned} \quad (\text{D2})$$

where α is the Gilbert damping constant.

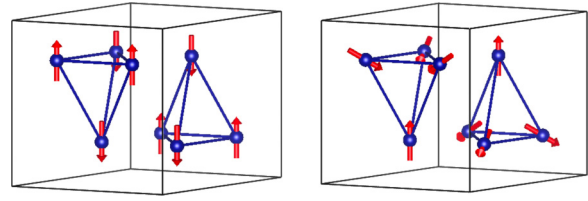


FIG. 12. Examples of initial spin configurations used for spin dynamics simulations by the LLG equation. $2 \times 2 \times 1$ supercell of the unit cell is considered.

We investigated the effects of the biquadratic term in the spin Hamiltonian by changing the initial spin configurations and the sign of the coefficients B_{ij} . As the initial spin configurations, the collinear AFM state and the noncoplanar AFM state in Fig. 12 are included. In the simulations, we set $\alpha = 0.1$, $k_B T = 0$ meV, $\Delta t = 1\hbar/\text{meV}$, and the total time length to be $1.5193 \times 10^3 \hbar/\text{meV}$. In addition, for simplicity, we fix the nearest-neighbor J_{ij} as -1.0 meV for both interlayer and intralayer directions and we also set the magnitude of the biquadratic term $|B_{ij}|$ to be the same as 0.1 meV for both directions. According to the simulations, the collinear AFM state was stabilized if $B > 0$; otherwise, a noncoplanar AFM state was stabilized. The results did not depend on the magnitude of the biquadratic term. Therefore we can conclude that the sign of the biquadratic term is crucial to break the degeneracy of the collinear AFM and noncoplanar AFM. First-principles derivation of higher-order interactions [59,60], such as the biquadratic interaction, is left for future work.

-
- [1] T. Chowdhury, E. C. Sadler, and T. J. Kempa, Progress and prospects in transition-metal dichalcogenide research beyond 2D, *Chem. Rev.* **120**, 12563 (2020).
- [2] X. Yin, C. S. Tang, Y. Zheng, J. Gao, J. Wu, H. Zhang, M. Chhowalla, W. Chen, and A. T. S. Wee, Recent developments in 2D transition metal dichalcogenides: Phase transition and applications of the (quasi-)metallic phases, *Chem. Soc. Rev.* **50**, 10087 (2021).
- [3] W. Choi, N. Choudhary, G. H. Han, J. Park, D. Akinwande, and Y. H. Lee, Recent development of two-dimensional transition metal dichalcogenides and their applications, *Mater. Today* **20**, 116 (2017).
- [4] S. Manzeli, D. Ovchinnikov, D. Pasquier, O. V. Yazyev, and A. Kis, 2d transition metal dichalcogenides, *Nat. Rev. Mater.* **2**, 17033 (2017).
- [5] T. Moriya and T. Miyadai, Evidence for the helical spin structure due to antisymmetric exchange interaction in $\text{Cr}_{1/3}\text{NbS}_2$, *Solid State Commun.* **42**, 209 (1982).
- [6] A. F. Gubkin, E. P. Proskurina, Y. Kousaka, E. M. Sherokolova, N. V. Selezneva, P. Miao, S. Lee, J. Zhang, Y. Ishikawa, S. Torii, T. Kamiyama, J. Campo, J. Akimitsu, and N. V. Baranov, Crystal and magnetic structures of $\text{Cr}_{1/3}\text{NbSe}_2$ from neutron diffraction, *J. Appl. Phys.* **119**, 013903 (2016).
- [7] L. M. Volkova and D. V. Marinin, Role of structural factors in formation of chiral magnetic soliton lattice in $\text{Cr}_{1/3}\text{NbS}_2$, *J. Appl. Phys.* **116**, 133901 (2014).
- [8] Y. Togawa, T. Koyama, K. Takayanagi, S. Mori, Y. Kousaka, J. Akimitsu, S. Nishihara, K. Inoue, A. S. Ovchinnikov, and J. Kishine, Chiral Magnetic Soliton Lattice on a Chiral Helimagnet, *Phys. Rev. Lett.* **108**, 107202 (2012).
- [9] Y. Kousaka, Y. Nakao, J. Kishine, M. Akita, K. Inoue, and J. Akimitsu, Chiral helimagnetism in $T_{1/3}\text{NbS}_2$ ($T = \text{Cr}$ and Mn), *Nucl. Instrum. Methods Phys. Res., Sect. A* **600**, 250 (2009).
- [10] D. Obeysekera, K. Gamage, Y. Gao, S.-w. Cheong, and J. Yang, The magneto-transport properties of $\text{Cr}_{1/3}\text{TaS}_2$ with chiral magnetic solitons, *Adv. Electron. Mater.* **7**, 2100424 (2021).
- [11] W.-H. Xie, B.-G. Liu, and D. G. Pettifor, Half-metallic ferromagnetism in transition metal pnictides and chalcogenides with wurtzite structure, *Phys. Rev. B* **68**, 134407 (2003).
- [12] S. S. P. Parkin, E. A. Marseglia, and P. J. Brown, Magnetic structure of $\text{Co}_{1/3}\text{NbS}_2$ and $\text{Co}_{1/3}\text{TaS}_2$, *J. Phys. C* **16**, 2765 (1983).
- [13] H. Y. Lv, W. J. Lu, D. F. Shao, Y. Liu, and Y. P. Sun, Strain-controlled switch between ferromagnetism and antiferromagnetism in $1T\text{-CrX}_2$ ($X = \text{Se}, \text{Te}$) monolayers, *Phys. Rev. B* **92**, 214419 (2015).
- [14] Y. Yamasaki, R. Moriya, M. Arai, S. Masubuchi, S. Pyon, T. Tamegai, K. Ueno, and T. Machida, Exfoliation and van der Waals heterostructure assembly of intercalated ferromagnet $\text{Cr}_{1/3}\text{TaS}_2$, *2D Mater.* **4**, 041007 (2017).

- [15] X. Zhao, P. Song, C. Wang, A. C. Riis-Jensen, W. Fu, Y. Deng, D. Wan, L. Kang, S. Ning, J. Dan, T. Venkatesan, Z. Liu, W. Zhou, K. S. Thygesen, X. Luo, S. J. Pennycook, and K. P. Loh, Engineering covalently bonded 2D layered materials by self-intercalation, *Nature (London)* **581**, 171 (2020).
- [16] P. Park, Y.-G. Kang, J. Kim, K. H. Lee, H.-J. Noh, M. J. Han, and J.-G. Park, Field-tunable toroidal moment and anomalous Hall effect in noncollinear antiferromagnetic Weyl semimetal $\text{Co}_{1/3}\text{TaS}_2$, *npj Quantum Mater.* **7**, 42 (2022).
- [17] S. Mangelsen, J. Hansen, P. Adler, W. Schnelle, W. Bensch, S. Mankovsky, S. Polesya, and H. Ebert, Large anomalous Hall effect and slow relaxation of the magnetization in $\text{Fe}_{1/3}\text{TaS}_2$, *J. Phys. Chem. C* **124**, 24984 (2020).
- [18] J. G. Checkelsky, M. Lee, E. Morosan, R. J. Cava, and N. P. Ong, Anomalous Hall effect and magnetoresistance in the layered ferromagnet $\text{Fe}_{1/4}\text{TaS}_2$: The inelastic regime, *Phys. Rev. B* **77**, 014433 (2008).
- [19] L. Šmejkal, R. González-Hernández, T. Jungwirth, and J. Sinova, Crystal time-reversal symmetry breaking and spontaneous Hall effect in collinear antiferromagnets, *Sci. Adv.* **6**, eaaz8809 (2020).
- [20] H. Park, O. Heinonen, and I. Martin, First-principles study of magnetic states and the anomalous Hall conductivity of MNb_3S_6 ($M = \text{Co}, \text{Fe}, \text{Mn}, \text{and Ni}$), *Phys. Rev. Mater.* **6**, 024201 (2022).
- [21] S. Mankovsky, S. Polesya, H. Ebert, and W. Bensch, Electronic and magnetic properties of $2H\text{-NbS}_2$ intercalated by $3d$ transition metals, *Phys. Rev. B* **94**, 184430 (2016).
- [22] M.-T. Huebsch, T. Nomoto, M.-T. Suzuki, and R. Arita, Benchmark for *Ab Initio* Prediction of Magnetic Structures Based on Cluster-Multipole Theory, *Phys. Rev. X* **11**, 011031 (2021).
- [23] A. I. Liechtenstein, M. I. Katsnelson, and V. A. Gubanov, Exchange interactions and spin-wave stiffness in ferromagnetic metals, *J. Phys. F* **14**, L125 (1984).
- [24] A. Sakuma, First principles study on the exchange constants of the $3d$ transition metals, *J. Phys. Soc. Jpn.* **68**, 620 (1999).
- [25] A. Sakuma, First-principles study on the non-collinear magnetic structures of disordered alloys, *J. Phys. Soc. Jpn.* **69**, 3072 (2000).
- [26] T. Nomoto, T. Koretsune, and R. Arita, Local force method for the *ab initio* tight-binding model: Effect of spin-dependent hopping on exchange interactions, *Phys. Rev. B* **102**, 014444 (2020).
- [27] T. Nomoto, T. Koretsune, and R. Arita, Formation Mechanism of the Helical \mathbf{Q} Structure in Gd-Based Skyrmion Materials, *Phys. Rev. Lett.* **125**, 117204 (2020).
- [28] Y. Nomura, T. Nomoto, M. Hirayama, and R. Arita, Magnetic exchange coupling in cuprate-analog d^9 nickelates, *Phys. Rev. Res.* **2**, 043144 (2020).
- [29] G. Kresse and J. Furthmüller, Efficient iterative schemes for *ab initio* total-energy calculations using a plane-wave basis set, *Phys. Rev. B* **54**, 11169 (1996).
- [30] J. P. Perdew, K. Burke, and M. Ernzerhof, Generalized Gradient Approximation Made Simple, *Phys. Rev. Lett.* **77**, 3865 (1996).
- [31] P. E. Blöchl, Projector augmented-wave method, *Phys. Rev. B* **50**, 17953 (1994).
- [32] G. Kresse and D. Joubert, From ultrasoft pseudopotentials to the projector augmented-wave method, *Phys. Rev. B* **59**, 1758 (1999).
- [33] G. Pizzi, V. Vitale, R. Arita, S. Blügel, F. Freimuth, G. Géranton, M. Gibertini, D. Gresch, C. Johnson, T. Koretsune, J. Ibañez-Azpiroz, H. Lee, J.-M. Lihm, D. Marchand, A. Marrazzo, Y. Mokrousov, J. I. Mustafa, Y. Nohara, Y. Nomura, L. Paulatto *et al.*, Wannier90 as a community code: New features and applications, *J. Phys.: Condens. Matter* **32**, 165902 (2020).
- [34] H. Shinaoka, J. Otsuki, M. Ohzeki, and K. Yoshimi, Compressing Green's function using intermediate representation between imaginary-time and real-frequency domains, *Phys. Rev. B* **96**, 035147 (2017).
- [35] N. Chikano, K. Yoshimi, J. Otsuki, and H. Shinaoka, ir-basis: Open-source database and software for intermediate-representation basis functions of imaginary-time Green's function, *Comput. Phys. Commun.* **240**, 181 (2019).
- [36] A. E. Hall, D. D. Khalyavin, P. Manuel, D. A. Mayoh, F. Orlandi, O. A. Petrenko, M. R. Lees, and G. Balakrishnan, Magnetic structure investigation of the intercalated transition metal dichalcogenide $\text{V}_{1/3}\text{NbS}_2$, *Phys. Rev. B* **103**, 174431 (2021).
- [37] K. Lu, D. Sapkota, L. DeBeer-Schmitt, Y. Wu, H. B. Cao, N. Mannella, D. Mandrus, A. A. Aczel, and G. J. MacDougall, Canted antiferromagnetic order in the monoaxial chiral magnets $\text{V}_{1/3}\text{TaS}_2$ and $\text{V}_{1/3}\text{NbS}_2$, *Phys. Rev. Mater.* **4**, 054416 (2020).
- [38] S. Wu, Z. Xu, S. C. Haley, S. F. Weber, A. Acharya, E. Maniv, Y. Qiu, A. A. Aczel, N. S. Settineri, J. B. Neaton, J. G. Analytis, and R. J. Birgeneau, Highly Tunable Magnetic Phases in Transition-Metal Dichalcogenide $\text{Fe}_{1/3+\delta}\text{NbS}_2$, *Phys. Rev. X* **12**, 021003 (2022).
- [39] A. Little, C. Lee, C. John, S. Doyle, E. Maniv, N. L. Nair, W. Chen, D. Rees, J. W. F. Venderbos, R. M. Fernandes, J. G. Analytis, and J. Orenstein, Three-state nematicity in the triangular lattice antiferromagnet $\text{Fe}_{1/3}\text{NbS}_2$, *Nat. Mater.* **19**, 1062 (2020).
- [40] P. Popčević, Y. Utsumi, I. Biało, W. Tabis, M. A. Gala, M. Rosmus, J. J. Kolodziej, N. Tomaszewska, M. Garb, H. Berger, I. Batišić, N. Barišić, L. Forró, and E. Tutiš, Role of intercalated cobalt in the electronic structure of $\text{Co}_{1/3}\text{NbS}_2$, *Phys. Rev. B* **105**, 155114 (2022).
- [41] N. J. Ghimire, A. S. Botana, J. S. Jiang, J. Zhang, Y. S. Chen, and J. F. Mitchell, Large anomalous Hall effect in the chiral-lattice antiferromagnet CoNb_3S_6 , *Nat. Commun.* **9**, 3280 (2018).
- [42] C. Battaglia, H. Cercellier, L. Despont, C. Monney, M. Prester, H. Berger, L. Forró, M. G. Garnier, and P. Aebi, Non-uniform doping across the Fermi surface of NbS_2 intercalates, *Eur. Phys. J. B* **57**, 385 (2007).
- [43] J. M. Vandenberg-Voorhoeve, Structural and magnetic properties of layered chalcogenides of the transition elements, in *Optical and Electrical Properties*, edited by P. A. Lee (Springer Netherlands, Dordrecht, 1976), pp. 423–457.
- [44] H. Zhang, W. Wei, G. Zheng, J. Lu, M. Wu, X. Zhu, J. Tang, W. Ning, Y. Han, L. Ling, J. Yang, W. Gao, Y. Qin, and M. Tian, Electrical and anisotropic magnetic properties in layered $\text{Mn}_{1/3}\text{TaS}_2$ crystals, *Appl. Phys. Lett.* **113**, 072402 (2018).
- [45] S. S. P. Parkin and R. H. Friend, $3d$ transition-metal intercalates of the niobium and tantalum dichalcogenides. ii. Transport properties, *Philos. Mag. B* **41**, 95 (1980).
- [46] B. Van Laar, H. Rietveld, and D. Ijdo, Magnetic and crystallographic structures of Me_xNbS_2 and Me_xTaS_2 , *J. Solid State Chem.* **3**, 154 (1971).

- [47] Y. Ōnuki, K. Ina, T. Hirai, and T. Komatsubara, Magnetic properties of intercalation compound: $Mn_{1/4}MX_2$, *J. Phys. Soc. Jpn.* **55**, 347 (1986).
- [48] A. Rahman, M. U. Rehman, M. Yousaf, M. Kiani, H. Zhao, J. Wang, Y. Lu, K. Ruan, R. Dai, Z. Wang, W. Liu, L. Zhang, and Z. Zhang, RKKY-type in-plane ferromagnetism in layered $Mn_{1/4}NbS_2$ single crystals, *Phys. Rev. B* **105**, 214410 (2022).
- [49] O. Gorochoy, A. L. Blanc-soreau, J. Rouxel, P. Imbert, and G. Jehanno, Transport properties, magnetic susceptibility and Mössbauer spectroscopy of $Fe_{0.25}NbS_2$ and $Fe_{0.33}NbS_2$, *Philos. Mag. B* **43**, 621 (1981).
- [50] T. Tsuji, Y. Yamamura, M. Koyano, S. Katayama, and M. Ito, Thermodynamic and magnetic properties of intercalated layered compounds Fe_xNbS_2 , *J. Alloys Compd.* **317-318**, 213 (2001), the 13th International Conference on Solid Compounds of Transition Elements.
- [51] J. Voorhoeve-van Den Berg and R. Sherwood, Low-temperature magnetic susceptibilities of $NbSe_2$ containing the first-row transition metals, *J. Phys. Chem. Solids* **32**, 167 (1971).
- [52] S. S. P. Parkin and R. H. Friend, $3d$ transition-metal intercalates of the niobium and tantalum dichalcogenides. i. Magnetic properties, *Philos. Mag. B* **41**, 65 (1980).
- [53] E. Morosan, H. W. Zandbergen, L. Li, M. Lee, J. G. Checkelsky, M. Heinrich, T. Siegrist, N. P. Ong, and R. J. Cava, Sharp switching of the magnetization in $Fe_{1/4}TaS_2$, *Phys. Rev. B* **75**, 104401 (2007).
- [54] K.-T. Ko, K. Kim, S. B. Kim, H.-D. Kim, J.-Y. Kim, B. I. Min, J.-H. Park, F.-H. Chang, H.-J. Lin, A. Tanaka, and S.-W. Cheong, RKKY Ferromagnetism with Ising-Like Spin States in Intercalated $Fe_{1/4}TaS_2$, *Phys. Rev. Lett.* **107**, 247201 (2011).
- [55] N. Maksimovic, R. Day, N.-H. Jo, C. Jozwiak, A. Bostwick, A. Liebman-Peláez, F. Wan, E. Rotenberg, S. Griffin, J. Singleton, and J. G. Analytis, Strongly correlated itinerant magnetism on the boundary of superconductivity in a magnetic transition metal dichalcogenide, [arXiv:2208.9475](https://arxiv.org/abs/2208.9475).
- [56] A. Sakuma, Theoretical study on the exchange constants of the transition metal systems, *IEEE Trans. Magn.* **35**, 3349 (1999).
- [57] Y. M. Quan, L. J. Zou, D. Y. Liu, and H. Q. Lin, Competition between crystal field splitting and Hund's rule coupling in two-orbital magnetic metal-insulator transitions, *Eur. Phys. J. B* **85**, 55 (2012).
- [58] S. F. Weber and J. B. Neaton, Origins of anisotropic transport in the electrically switchable antiferromagnet $Fe_{1/3}NbS_2$, *Phys. Rev. B* **103**, 214439 (2021).
- [59] S. Mankovsky, S. Polesya, and H. Ebert, Extension of the standard Heisenberg Hamiltonian to multispin exchange interactions, *Phys. Rev. B* **101**, 174401 (2020).
- [60] A. Szilva, M. Costa, A. Bergman, L. Szunyogh, L. Nordström, and O. Eriksson, Interatomic Exchange Interactions for Finite-Temperature Magnetism and Nonequilibrium Spin Dynamics, *Phys. Rev. Lett.* **111**, 127204 (2013).